PHYSICAL REVIEW B **81**, 064419 (2010)

Ferromagnetism in SnO_2-based multilayers: Clustering of defects induced by doping

A. Espinosa,[1] M. García-Hernández,[1] N. Menéndez,[2] C. Prieto,[1] and A. de Andrés[1]
[1]*Instituto de Ciencia de Materiales de Madrid, Consejo Superior de Investigaciones Científicas, Cantoblanco, E-28049 Madrid, Spain*
[2]*Departamento de Química-Física Aplicada, Universidad Autónoma de Madrid, Cantoblanco, E-28049 Madrid, Spain*
(Received 24 September 2009; revised manuscript received 11 December 2009; published 19 February 2010)

Several series of A/SnO_2 and Mn/B multilayers, where A and B are thin layers (0.4–10.1 nm) of SnO_2, SiO_2, Si, Al, Mn, or MnO_x, have been investigated magnetic, electronic, and structurally. The study demonstrates that the detected ferromagnetism is related to regions of high density of defects in SnO_2 induced by doping under particular conditions. The observed room-temperature ferromagnetic (RTFM) signal does not scale to Mn content but increases with the number of interfaces and their roughness. The presence of Mn in 3+ oxidation state in the SnO_2 lattice is a necessary condition but is not enough to promote ferromagnetism which also requires the presence of Sn^{2+}. The high oxygen deficiency induced by Mn doping in the tin-oxide layers is mostly compensated by the formation of the stable SnO phase. Moreover, the RTFM signal decreases upon annealing either in O_2 rich or in vacuum atmospheres. The combination of Mn with SiO_2, Si, or Al produces paramagnetic signals but no ferromagnetism; consequently SnO_2 is a crucial ingredient of this RTFM. The observed ferromagnetism may be explained by short-range ferromagnetic correlations between Mn probably mediated by induced holes at oxygen sites of SnO_2 in the vicinity of trivalent Mn^{3+} doping ions. The inhomogeneous Mn distribution inside tin oxide at the multilayer interfaces may produce large enough regions with high defect concentration to allow long-range ferromagnetic order. All undoped SnO_2 films, grown in a wide set of different conditions, show paramagnetic signals with high-J values but no ferromagnetism is detected probably because of the high density of defects required to establish a ferromagnetic order based in a short-range mechanism.

DOI: 10.1103/PhysRevB.81.064419 PACS number(s): 75.50.Pp, 71.23.Cq, 75.70.−i

I. INTRODUCTION

The understanding of ferromagnetism (FM) in magnetic oxides, wide gap oxides (ZnO, SnO_2, and TiO_2) doped with transition-metal (TM) ions (as Mn, Co, Fe, Cr, Ni, V, etc.), remains a challenge both from theoretical and experimental viewpoints. The existence of room-temperature ferromagnetism (RTFM) in doped TiO_2,[1,2] ZnO,[3,4] or SnO_2 (Refs. 5–10) systems has been reported. However, not only the origin of this ferromagnetism is still under debate, also diverse experimental results have been obtained for nominally the same compounds. The formation of ferromagnetic metallic clusters,[11,12] secondary phases,[13] or new metastable phases, as well as the presence of interfaces[14,15] and structural point defects,[16–18] are known to be relevant. Moreover, FM has been also reported in several nondoped oxides[19–21] when prepared as thin layers.

Several theories have been developed recently trying to explain the mechanism responsible of RTFM in oxides. The long-range interaction required to explain ferromagnetism in diluted systems has been accounted for either by free-carrier mediated exchange[22] or by the bound magnetic polarons (BMP) theory in semiconductors.[23] The BMP model has been used to describe the ferromagnetic order in oxides,[24] with or without transition-metal doping, and is related to the presence of donor electrons associated to oxygen vacancies, which are believed to be common in the chemistry of these oxides, forming magnetic polarons of a certain diameter that may percolate above a critical concentration of defects.

Among these oxides, tin oxide, SnO_2 has important applications in other fields, for example, as transparent conducting electrode in solar cells[25] or gas sensor[26] due its high optical transparency. However, in comparison with other oxides, there have been fewer reports on TM-doped SnO_2 but some with impressive ferromagnetic transition temperature, T_C, and magnetic moment per TM. In 2003, Ogale *et al.*[5] reported, in Co-doped SnO_2 films fabricated with pulse laser deposition (PLD), a giant magnetic moment ($7.5 \pm 0.5\mu_B/\text{Co}$) and high-$T_C$ (~ 650 K). Coey *et al.*[6] investigated 5% Fe-doped SnO_2 films also grown with PLD and revealing RTFM with a magnetic moment of $1.8\mu_B/\text{Fe}$. Lower magnetic moments have been observed in $Sn_{1-x}Co_xO_2$ powders.[7]

In the case of Mn-doped SnO_2, first investigations pointed out to a paramagnetic (PM) behavior in $Sn_{0.95}Mn_{0.05}O_2$ epitaxial films.[27] Coey *et al.*[24] presented a compendium of published results showing the dispersion of the magnetic moments per TM obtained in these oxides which, for Mn, varied, at that moment, from almost 0 to $\sim 6.8\mu_B/\text{Mn}$. Fitzgerald *et al.*[8] observed RTFM for the same system with an exceptionally high magnetic moment ($\sim 20\mu_B/\text{Mn}$), for a 1% of doping, which they attributed to the BMP mechanism. Later, other results reporting RTFM have been published for polycrystalline Mn-doped SnO_2 films with magnetic moments of $0.18\mu_B/\text{Mn}$ (Ref. 9) and of $3\mu_B/\text{Mn}$,[10] this last report suggesting free-carrier mediated mechanism. The observed ferromagnetism in different magnetic oxides has been recursively related to the presence of oxygen vacancies also in oxides without TM doping[19,20] or in nanoparticles.[28]

Focusing on tin oxides, even the origin of conductivity of undoped SnO_2 is still controversial. Its n-type conductivity has been related to its intrinsic nonstoichiometry with oxygen vacancies (V_O) and tin interstitials (Sn_i) that donate electrons to the conduction band maintaining its transparency.[29] When analyzing SnO_2-based magnetic oxides, it is important to keep in mind that Sn has the particularity of forming two stable oxides SnO_2 (with Sn^{4+}) and SnO (Sn^{2+}). In fact, depending on the oxygen-rich or oxygen-poor conditions, the coupling of a divalent Sn interstitial (Sn_i^{2+}) to an oxygen vacancy produces such rearrangement of the surrounding lattice that we can talk of SnO-like local phase.[29] In SnO lattice, under oxygen-rich conditions, tin vacancies are the dominant defect forming shallow acceptor states and therefore *p*-type conductivity.[30] Recent calculations show that intrinsic defects in SnO_2 would not contribute to the conductivity since the electrons are deeply trapped.[31] These authors propose unintentional *H* doping, either at interstitials or at oxygen sites, to provide the shallow donors. Regarding ferromagnetism, the latest calculations demonstrate that it may arise from cation vacancies such as in ZnO (Ref. 32) or in SnO_2 (ref. 33) but not from V_O. In SnO_2, these authors obtain ferro or antiferro (AF) coupling of the holes at the oxygen ions around two close Sn vacancies (V_{Sn}) depending on their spacing. The optimum situation for a ferro coupling corresponds to a distance of 5.5 Å between two V_{Sn}. The up to now published experimental results point to a dependence of the magnetic properties on the oxidizing or reducing conditions and treatments that rather seem to evidence the important role of oxygen vacancies.[19,34] *Ab initio* calculations in rutile TiO_2 indicate that oxygen vacancies favor the introduction of impurities in the host, increasing the magnetic moments, and that the obtained magnetic order is FM for Co and AF for Mn or Fe impurities.[35] In Fe:SnO_2 similar conclusions are obtained but the coupling is FM.[36]

In this study, we have obtained several series of A/B multilayers as well as SnO_2 films. Multilayers with extremely thin Mn layers (down to 0.4 nm) were obtained to favor the formation of possible metastable phases at the Mn/SnO_2 interfaces.[37] Our interest was to obtain the relevant parameters that promote the RTFM in order to enlighten the different possible mechanisms of this complicated sample and laboratory-dependent observed magnetism. The films grown at low sputtering power in Ar and at room temperature (RT), either on Si(100) or sapphire (R-cut), are amorphous while the introduction of oxygen, the increase in power or a higher substrate temperature promote the formation of SnO_2 nanocrystals.[38] Samples grown at 500 °C produce epitaxial films on sapphire and polycrystalline films on Si. Only amorphous films are ferromagnetic while epitaxial or polycrystalline films present a paramagnetic contribution that quantitatively does not correspond to the introduced concentration of metal.

Mn was chosen as the transition metal since none of its known oxides, nor its metallic phases, are ferromagnetic, except Mn_3O_4 with $T_c=44$ K. To elucidate the origin of the ferromagnetism, SnO_2 was substituted by SiO_2, Si and Al and Mn by MnO_x in the other series of multilayers. We will show that the ferromagnetic signal requires the presence of a sufficiently high density, at least locally, of defects in SnO_2 which are induced under certain conditions by Mn^{3+}. The ferromagnetic coupling is provided by the SnO_2 lattice while Mn is not able to promote such coupling in SiO_2.

II. EXPERIMENTAL DETAILS

We have obtained several series of (A/B) multilayers based on different combinations of SnO_2, SiO_2, Si, Al, MnO_x, and Mn layers (in particular, A/SnO_2: Mn/SnO_2, MnO_x/SnO_2, Si/SnO_2 and Mn/B: Mn/Si, Mn/SiO_2, Mn/Al) as well as SnO_2 single layers. The multilayers and films were deposited at RT onto Si(100) using a magnetron sputtering method either in dc or rf configuration depending on the electronic conductivity of the targets. SnO_2 and Mn_3O_4 targets were made out from high-purity powders (SnO_2 and MnO, respectively) and sintered at 1200 °C. Note that MnO powder, when sintered, transforms into Mn_3O_4 which is more stable in air, the other targets were obtained commercially. SnO_2, SiO_2, and MnO_x layers were deposited with rf sputtering at 10 W. Mn, Si, and Al were grown by dc sputtering. All layers were deposited with Ar as sputtering gas (5×10^{-3} mbar). No O_2 were introduced in the chamber in order to (i) not oxidize the Mn, which tends to loose its metallic nature and (ii) promote the oxygen vacancies in our system. The base pressure was 1×10^{-6} mbar. The nominal Mn, MnO_x, or Al layer thickness ranges from 0.4 up to 10 nm while SnO_2, Si, and SiO_2 thickness is maintained constant (around 3 nm). The total nominal thickness of the multilayers varies from 68.5 to 280 nm. SnO_2 films of thickness up to 200 nm were obtained as reference samples. Some of the samples were subjected to a thermal treatment in high vacuum or under O_2 flow atmosphere at 750 °C in order to study the role of oxygen vacancies and to enhance its crystallinity.

The films and multilayers have been very carefully magnetically characterized avoiding using at any step metallic, even nominally “nonmagnetic,” tools. The magnetic measurements were performed with a superconducting quantum interference device magnetometer and the samples were cut in the appropriate dimensions to fit into the straw. The removal of the substrate diamagnetic signal is always a delicate point, therefore, after subtracting the diamagnetic signal corresponding to the weight of the substrate (estimated from the measurement of a fresh substrate) a correction is done (in the range of 5%) in order to obtain a horizontal signal for the 300 K cycles which is afterwards used at the other temperatures. This is a good approach since the paramagnetic signal of such thin films is small enough to be negligible at 300 K.

X-ray absorption spectroscopy (XAS) measurements in fluorescence configuration at Mn *K*-edge ($E_0=6539$ eV) were obtained for most of the films and multilayers to obtain the Mn valence state. The experiments were done at BM25 beamline at the European Synchrotron Radiation Facility (ESRF). These XAS measurements allowed us to check for any contamination from elements close in Z to Mn, in particular, from Fe. We observed that no Fe contamination is present in the samples.

X-ray reflectivity (XRR) was performed to evaluate the thickness and roughness of the films as well as the quality of the multilayer interfaces. Simulations of XRR measurements were performed using SUPREX® program.[39] A detailed structural study has been performed by x-ray diffraction (XRD) both in our laboratories and at BM25 beamline (ESRF). Two configurations were used: the standard θ-2θ ($\lambda=1.5406$ Å) and the low-angle incidence configuration (grazing incidence geometry with incidence angle of 0.75°, at ESRF) at 14 keV ($\lambda=0.8857$ Å) in order to minimize substrate signal, especially important in amorphous films. Rutherford backscatter-

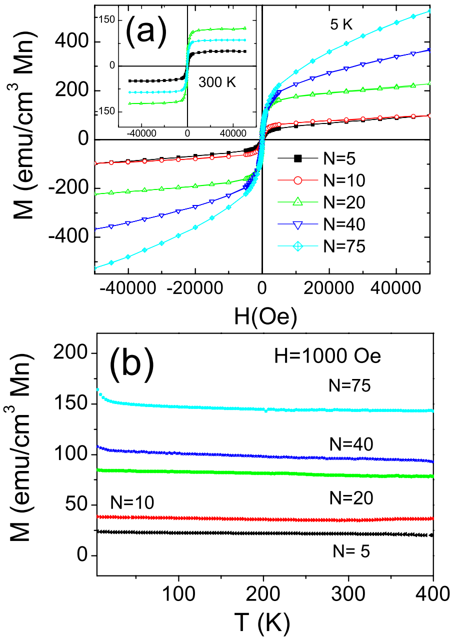

FIG. 1. (Color online) (a) Magnetization (M) vs magnetic field (H) at 5 K of Mn/SnO_2 multilayers with different number of bilayers N=5, 10, 20, 40, and 75. Inset: M vs H at 300 K of multilayers with N=5, 20, and 75 bilayers. (b) Magnetization (M) vs temperature (T) at 1000 Oe.

TABLE I. Parameters of Mn/SnO_2 multilayers: number of bilayers (N), Mn layer thickness (d_{Mn}), SnO_2 layer thickness (d_{SnO_2}), bilayer thickness ($d_{bilayer}$), interdiffusion thickness ($\sigma_{A\text{-}B}$), and percentage content of Mn. Parameters fitted with SUPREX (thickness error ~5%).

N bilayers	d_{Mn} (nm)	d_{SnO_2} (nm)	$d_{bilayer}$ (nm)	d_{total} (nm)	$\sigma_{A\text{-}B}$ (nm)	% Mn content
5	10.1	3.0	13.1	68.5	1.0	68
10	5.1	3.0	8.0	83.0	1.0	62
20	2.6	3.0	5.7	117.0	1.3	45
40	1.2	3.0	4.3	175.0	1.4	28
75[a]	0.7	3.0	3.7	280.5	1.5	19

[a] Extrapolated values.

ing (RBS) was performed at Centro de Microanálisis de Materiales (CMAM) using a 2 MeV $^4He^+$ ion beam in order to obtain a quantitative compositional characterization of the multilayers.

In order to obtain the local electronic state of Sn atoms into the multilayers, ^{119}Sn Mössbauer spectroscopy in emission mode was used. The spectra were recorded at room temperature in triangle mode, using a conventional Mössbauer spectrometer with Ca $^{119}SnO_3$ source on one end and ^{57}Co(Rh) source on the other end for energy calibration. The samples were placed in a He-4%CH_4 gas flow proportional counter to detect the internal-conversion electrons emitted by the ^{119}Sn nuclei after resonant absorption of gamma rays. The spectra were analyzed by a nonlinear fit using the NORMOS program.[40] The isomer shifts were referred to the Ca $^{119}SnO_3$ source.

III. DISCUSSION

Figure 1(a) shows the magnetization vs field at 5 K for the series of Mn/SnO_2 multilayers grown at RT that have been characterized by different techniques to obtain their structural and compositional properties (see Table I). The figure shows the presence, at 5 K, of ferromagnetic and paramagnetic components for all the samples. The inset shows the 300 K cycles of N=5, 20, and 75 multilayers and the lower part of Fig. 1 shows the field-cooled magnetization measured at 1000 Oe as a function of temperature. The figure demonstrates the presence of a ferromagnetic phase with $T_C > 400$ K, therefore RTFM.

The magnetization has been normalized to the volume of Mn estimated from the deposition rate, the fit of the XRR [Fig. 2(a)] and RBS data of some of the films [Fig. 2(c)]. XRR measurements and fits reveal an important roughness and interdiffusion ($\sigma_{A\text{-}B}$) between layers which is increased as the Mn layer thickness decreases (Table I). The simulations of the RBS spectra gave the atomic composition for N=5 and N=75 samples. The percentage of Mn, Sn, and O are 62%, 10%, and 28%, respectively, for N=5 multilayer, and 18%, 20%, and 62% for N=75 sample. The atomic Mn percentages coincide very well with the values obtained from the thicknesses of the layers. Figure 1 evidences that the magnetic signal is not proportional to the Mn content but rather seem to correlate to the number of bilayers N.

We have performed x-ray absorption and diffraction studies of the films with synchrotron radiation. Figure 2(b) shows the diffraction results for this series using fixed grazing incidence angle (around 0.75°) and varying the detector angle (2θ). The presence of MnO nanoclusters is detected [compare Fig. 2(b) and the MnO reference]. As N increases, the multilayers are such that the total amount of Mn is similar, but the SnO_2 total thickness ($=N \times d_{SnO_2}$) is proportional to N, therefore the intensity of the two bands, around 2.2 and 4 $Å^{-1}$ increases. In order to assign the origin of these bands, a SnO_2 undoped film was grown under the same conditions. Its diffractogram is similar to the N=75 multilayer (Fig. 3) but with slight differences. We will first mention that the band around 4 $Å^{-1}$ is in fact the combination of three components (as we could deduce after comparing a large number of different samples): one contribution at 3.8 $Å^{-1}$ arises from the SnO_2, and the other, at 3.95 $Å^{-1}$, from MnO nanoclusters and from a spurious band related to Si substrates. The two bands related to SnO_2 could be, in principle, originated from nanocrystals or/and amorphous SnO_2 or/and SnO.

As a first approach, SnO nanocrystals, rather than SnO_2, with mean size around 2 nm, would fit the results (compare the diffraction data of the films to those corresponding to 2 nm nanocrystals of both Sn oxides in Fig. 3) but Mössbauer spectroscopy demonstrates the exclusive presence of Sn^{4+} (Fig. 4) in SnO_2 films. The Mössbauer spectra of the as-grown films could be fitted as one quadrupole doublet with isomer shift δ=0.11 mm/s, quadrupole splitting Δ=0.80 mm/s, and linewidth, Γ=0.98, mm/s, indicative that these films are amorphous SnO_2, [Fig. 4(b)] contrary to the annealed films where Sn^{4+} has parameters,

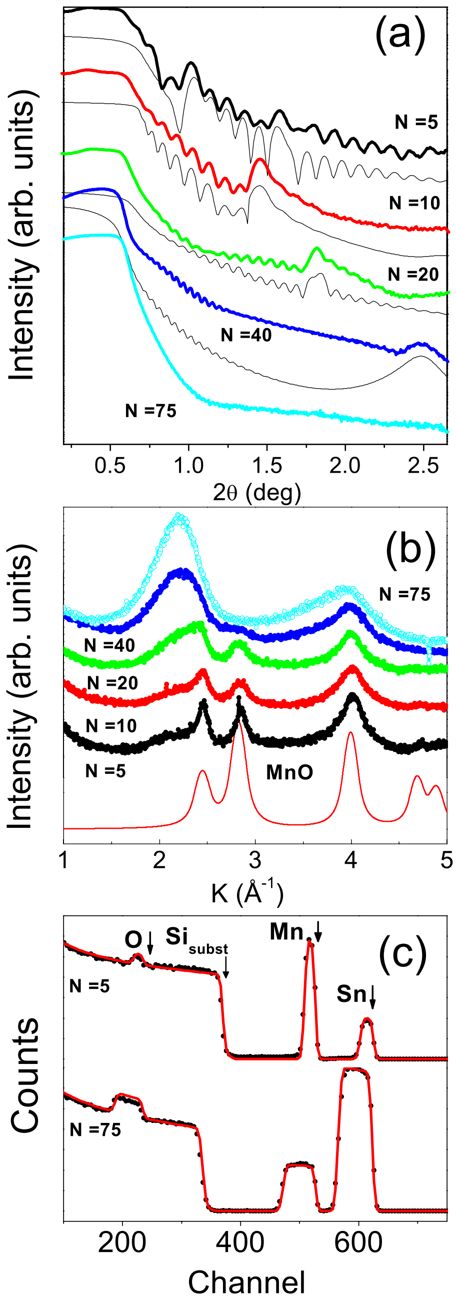

FIG. 2. (Color online) (a) X-ray reflectivity of Mn/SnO_2 multilayers with different number of bilayers $N=5$, 10, 20, 40, and 75. SUPREX simulations of reflectivity are also displayed. (b) XRD patterns ($l=0.885$ Å) at grazing incidence angle. MnO reference pattern is displayed below. (c) RBS spectra and simulations of multilayers with $N=5$ and 75 bilayers.

$\delta=0,01$ mm/s, $\Delta=0.45$ mm/s, and $\Gamma=0.78$ mm/s, of a crystalline environment according to.[41] Nevertheless, and this is a crucial point, Mössbauer also showed the presence of about 30 % of Sn^{2+} in the Mn/SnO_2 multilayers [Fig. 4(c), lower curve].

Coming back to diffraction, we have simulated the signal corresponding to randomly oriented SnO_6 and SnO_4 units (Fig. 3).[43] The SnO_6 units correspond to the octahedra and distances of crystalline SnO_2 while SnO_4 units correspond to tetrahedra in SnO crystal. Clearly none of these units do

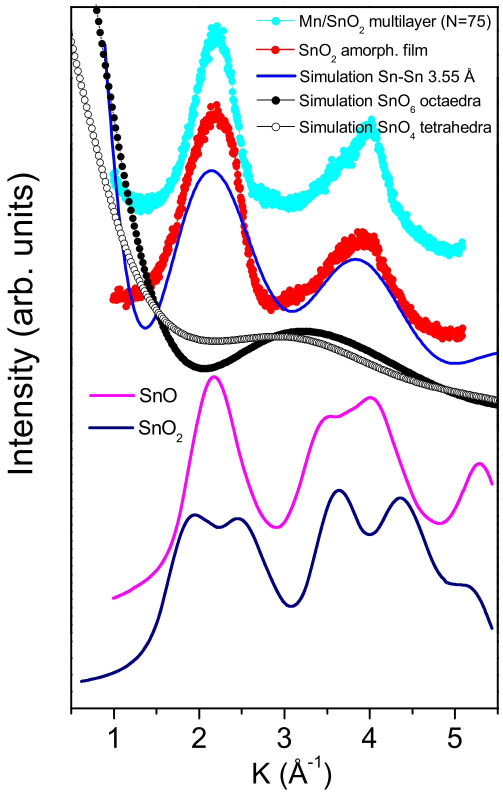

FIG. 3. (Color online) XRD data of SnO_2 film and Mn/SnO_2 multilayer of $N=75$ are displayed in the upper part with simulations of amorphous films considering SnO_6 octahedra, SnO_4 tetrahedral, and Sn-Sn pairs (3.55 Å). Lower part: SnO and SnO_2 diffraction patterns corresponding to 2 nm nanocrystals.

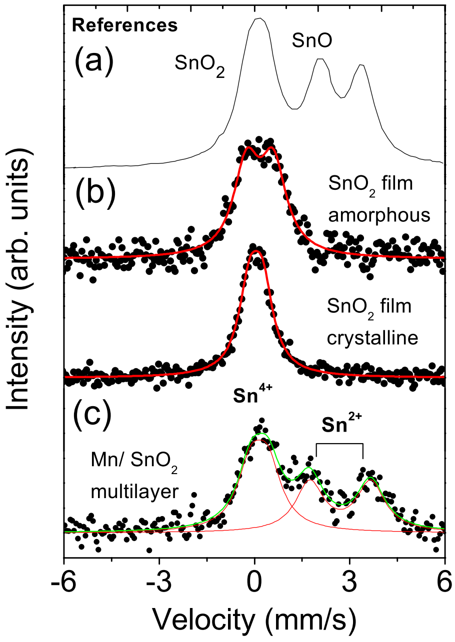

FIG. 4. (Color online) (a) Mössbauer spectra of a reference sample of mixed SnO_2 and SnO oxides (Ref. 42). (b) Measured spectra of undoped SnO_2 amorphous (as grown) and crystalline (annealed) 200 nm films. (c) Mössbauer spectra of the $N=75$ Mn/SnO_2 multilayer ($N=75$).

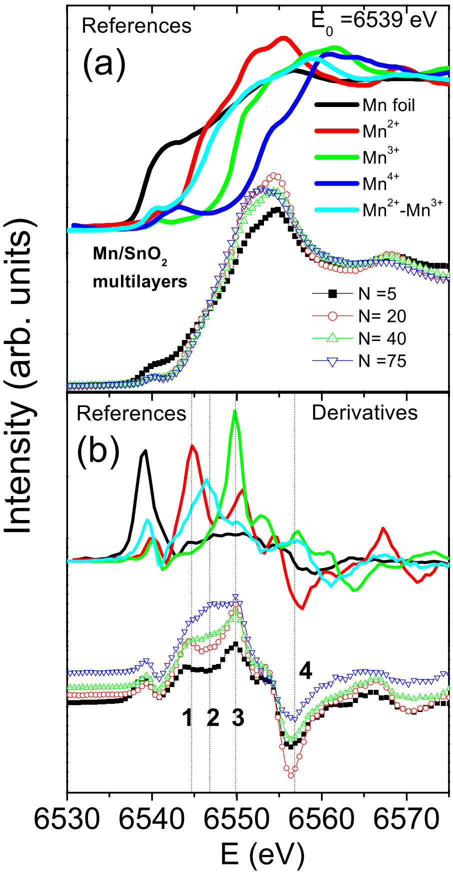

FIG. 5. (Color online) (a) Mn *K*-edge XANES spectra for reference Mn oxides (metallic Mn, MnO:Mn^{2+}, Mn_2O_3:Mn^{3+}, MnO_2:Mn^{4+}, and Mn_3O_4:Mn^{2+}-Mn^{3+}) and for as-grown Mn/SnO_2 multilayers (N=5, 20, 40, and 75 bilayers). (b) Derivatives of the above signals.

originate the observed data. The observed bands are due to Sn-Sn pairs (Fig. 3) at a distance around 3.55 Å. This distance is close to Sn-Sn distances present in both tin oxides. Therefore, we can conclude that SnO_2 films grown at RT are amorphous with Sn-Sn distances close to the crystal values but where the angles Sn-O-Sn have a certain distribution so that the long-range order is lost. Looking at the multilayers, it is clear that the diffraction bands are narrower than those of SnO_2 films. Therefore, we propose that the multilayers contain a combination of SnO_2 and SnO mainly in amorphous phase with some contribution of nanocrystalline (around 2 nm) phases.

Finally, XAS spectra at Mn *K* edge of the series of Mn/SnO_2 multilayers [Fig. 5(a)] are presented and compared to reference Mn oxides and α-Mn (metal). The first observation is that the spectra do not correspond to a unique valence state of Mn. The only multilayer that presents a significant content of metallic Mn is the one with the thicker Mn layers (d_{Mn}=10.2 nm and N=5). Figure 5(b) shows the derivatives of the spectra of the reference compounds and of the samples. The maxima in the derivatives correspond to inflexion points of the XAS signals which characterize the valence states of Mn. The dashed vertical lines labeled with **1** and **4** correspond to features of MnO (Mn^{2+}), the labeled with **3** to Mn_2O_3 (Mn^{3+}) and that labeled as **2** to Mn_3O_4 (33% of Mn^{2+} and 67% of Mn^{3+}). It results that all samples contain Mn^{2+} and Mn^{3+}, and that a component (**2**) similar to the combination of Mn^{2+} and Mn^{3+} appears as the number of Mn layers increases and their thickness decreases. Concomitantly, the feature **4** (related to Mn^{2+}) decreases. Mn^{2+} corresponds to the detected MnO nanocrystals by diffraction while there is no indication of any crystalline phase related to Mn^{3+}.

Once the samples have been thoroughly characterized, we come back to magnetic data. We fitted the signal for the series of multilayers using a combination of Brillouin functions to take into account the paramagnetic and ferromagnetic components. The ferromagnetic contribution can be approximated to a Brillouin function with a large enough angular momentum J [we have taken $J_{\mathrm{FM}}=100$ (Ref. 44)] while J of the paramagnetic part, J_{PM}, is a fitting parameter. For all multilayers, and especially for those with low N, the obtained J_{PM} values are very small (<0.5) and lack of physical meaning if the magnetic moments are related to Mn ions: the standard J_{PM} values should vary from 1.5 to 2.5, for Mn^{4+} to Mn^{2+}, respectively. We have therefore included an antiferromagnetic component since XRD measurements revealed the presence of MnO nanocrystals which are antiferromagnetic with $T_N \sim 120$ K. In antiferromagnets, the magnetization dependence with H is almost linear and, in MnO, the slope for a measured reference sample was 4.3×10^{-4} (emu/Oe cm^3). So we will take into account three different contributions for the fit: FM, PM, and AF,

$$M(H,T,J) = \mathrm{AF}\cdot 4.35\times10^{-4}\cdot H + \mathrm{FM}\cdot B_j(H,T,J_{\mathrm{FM}}) + \mathrm{PM}\cdot B_j(H,T,J_{\mathrm{PM}}) \quad (\mathrm{emu/cm^3}),$$

where AF, FM, and PM are the coefficients of the different components, $\mathrm{PM}=\frac{N}{V} g\mu_B J_{\mathrm{PM}}$, $B_J(H,T,J)$ is the Brillouin function and N/V the density of magnetic centers.

AF components produce very small signals and the parameters of the paramagnetic and antiferromagnetic phases are correlated so, finally, we fixed the AF weight (AF=1), and $J_{\mathrm{PM}}=2$ [Mn^{3+}, consistent with x-ray appearance near-edge structure (XANES) results] to fit all the series and left the PM and FM fractions as the fitting parameters. Figure 6(a) shows the measured and fitted magnetic cycles of N=40 sample at 5 and 300 K. In Figs. 6(c) and 6(d), the FM and PM fractions are plotted, both in emu/cm^3 Mn and emu/cm^3(total). We can observe that neither the FM nor PM signals are proportional to the Mn content but, as the number of interfaces (2N) increases, both contributions increase. Clearly the number of interfaces is favoring the ferromagnetic and paramagnetic components. Unfortunately, from these fits we cannot determine, within a reasonable error, the AF part which would allow estimating the fraction of Mn in FM and PM phases. All samples have an important antiferromagnetic component and most probably, the increase in the FM and PM signals is due to the reduction in MnO oxide (as indicated by XANES) and increase the fraction of Mn inside the SnO lattice favored by the number and roughness of interfaces. Note that N=75 sample does not show the MnO diffraction peaks [Fig. 2(b)] but AF coupling persists. The corresponding moments per Mn of the ferromagnetic signal

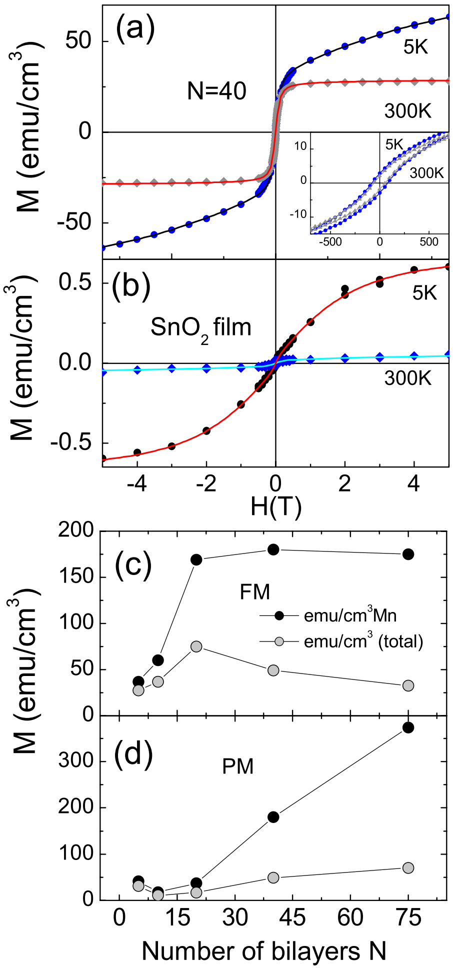

FIG. 6. (Color online) Magnetization (M) vs magnetic field (H) at 5 and 300 K of (a) the Mn/SnO$_2$ multilayer with $N=40$. The lines are fits using a combination of Brillouin functions and an AF component and (b) an undoped amorphous SnO$_2$ film. Coefficients of the ferromagnetic (c) and paramagnetic (d) components along the series in emu/cm^3 and in emu/cm^3 Mn.

range from 0.06 to $0.24\mu_B$/at Mn at 5 K and $0.01-0.2\mu_B$/at Mn at 300 K but it is to note that, in fact, only a small fraction of Mn is contributing to the FM signal, therefore the actual moments per Mn have to be much higher.

The magnetic signal of an as-grown undoped SnO$_2$ film is shown in Fig. 6(b). The obtained signal at 5 K and 5 T is around 100 times smaller than those corresponding to the multilayers [$N=40$, Fig. 6(a)]. For the undoped film we have obtained, apart from a very weak ferromagnetic contribution that we do not consider relevant, a paramagnetic behavior (see continuous line in the figure) with $J_{\mathrm{PM}}=3.2$. To check the validity of the fit, we simulate the signal at 300 K with the parameters obtained at 5 K resulting in perfect agreement with the data. Therefore, the SnO$_2$ films do present a weak paramagnetic signal indicating the presence of magnetic centers that, according to the calculations,[33] would be related to Sn vacancies. The J value around 3 is quite large (for example, this can correspond to 6 electrons or holes with spin $\frac{1}{2}$) and the number of these centers per cm^3 is (taking $g=2$) about 10^{19}, which means that there is 1 magnetic center per 1000 SnO$_2$ unit cells. To obtain a cooperative ferromagnetic signal, not only the interaction between centers has to be ferromagnetic, also, the density of centers has to be high for short-range mechanisms. Considering the calculated distance for a ferromagnetic coupling between Sn vacancies [around 5 Å (Ref. 33)), the density obtained here is clearly too low. On the contrary, at the interfaces of the multilayers, the number of magnetic centers may be high enough to form ferromagnetic regions or clusters.

Summarizing the results on the Mn/SnO$_2$ multilayers, it is well established that they contain both Sn^{4+} and Sn^{2+}, with Sn-Sn distances typical for any of the stable tin oxides (around 3.55 Å) with a dispersion of Sn-O-Sn angles that breaks the structural long-range order. Mn is present in different valence states: metallic Mn (only for the thickest Mn layer), Mn^{2+} (corresponding to MnO) and Mn^{3+} most probably inside the Sn oxides at the interfaces. The ferromagnetic signal does not scale to the Mn content and the maximum value corresponds to an optimum combination of number of layers and Mn layer thickness. An antiferromagnetic component is always present related to MnO. The paramagnetic component clearly increases for ultrathin Mn layers and large N. Remembering that XRR indicates an important roughness and interdiffusion of Mn/SnO$_2$ interfaces we may conclude that both ferromagnetic and paramagnetic signals correspond to these Sn-O-Mn^{3+} regions at the interfaces.

In order to check if the magnetic signal is related to some unstable, distorted, or nonstoichiometric Mn oxide, we have fabricated another series of multilayers combining Mn with SnO$_2$, SiO$_2$, Si, and Al (all with thickness of both types of layers around 3 nm) with $N=20$ bilayers. The magnetic signal for all of them, except for Mn/SnO$_2$, corresponds either to weak paramagnetic or AF behaviors [Fig. 7(a)]. All contain metallic Mn but with decreasing proportions following the sequence: Mn/Al, Mn/Si, and Mn/SiO$_2$ multilayers. Mn/SiO$_2$ also contains Mn with valences 2+ and 3+. Therefore the presence of Mn and oxygen with different valences is not sufficient to obtain a ferromagnetic phase.

To evaluate the relevance of oxygen vacancies in the magnetism, we have proceeded to anneal the multilayers at temperatures around 750 °C either in vacuum (reducing atmosphere) or in O$_2$-rich atmosphere. The effect of annealing treatments is to crystallize the SnO$_2$ and SnO oxides and to form Mn$_2$O$_3$ and Mn$_3$O$_4$ oxides [Figs. 8(a) and 8(b)]. Annealing in reducing or oxidizing atmospheres modifies the magnetic signal decreasing drastically the RTFM and appearing a ferromagnetic signal related to Mn$_3$O$_4$ in both cases [Figs. 8(c) and 8(d)]. The difference related to the annealing atmospheres lies in the degree of crystallization of the nanocrystals and in the permanence of a small fraction of tin mono-oxide, SnO, when annealing in vacuum. Figures 8(a) and 8(b) shows the diffraction data of two multilayers annealed one in O$_2$-rich atmosphere and the other in vacuum, respectively. In the second case, the formation of SnO$_2$ as well as Mn$_2$O$_3$ and Mn$_3$O$_4$ is evidenced but the background indicates that a fraction of amorphous material remains. In the first case (note that the proportion of nominal Mn and SnO$_2$ content is different in both multilayers), the exclusive formation of SnO$_2$ is clear as well as the formation of the same Mn oxides. The ferromagnetic signal is almost identi-

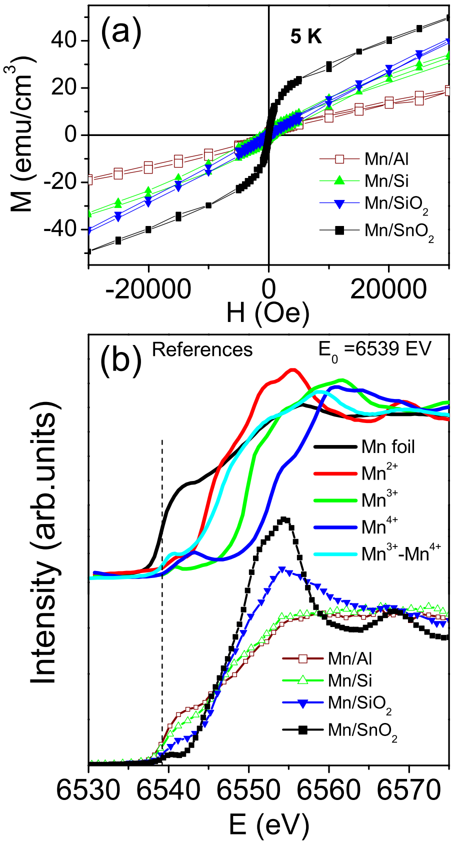

FIG. 7. (Color online) (a) Magnetization, in emu/cm^3 vs magnetic field applied parallel to the film plane at 5 K for the series $(Mn/B)_{20}$, where $B:SiO_2$, Si, Al, and SnO_2 with $N=20$ bilayers (b) Mn *K*-edge XANES spectra for reference Mn oxides (metallic Mn, Mn^{2+}, Mn^{3+} and Mn^{4+}) and for Mn/B multilayers.

cal in both cases and is dominated by the presence of Mn_3O_4 which is ferromagnetic at $T_c=44$ K [see insets of Figs. 8(c) and 8(d)] and presents a high coercive field due to its nanometric size. Mössbauer spectroscopy confirms the disappearance of Sn^{2+} when annealing in O_2 [Figs. 9(a) and 9(b)]. Therefore, annealing in reducing or oxidizing atmospheres decreases the room-temperature ferromagnetic signal.

Looking at Mn *K* edge it is clear that the contribution of higher Mn valence states is increased both for O_2 and vacuum annealed samples [Fig. 8(e)]. Therefore annealing does not promote the formation of mixed Sn-Mn oxides but transforms the samples so that stable tin and Mn oxides are formed and the RTFM is destroyed.

We fabricated another series of multilayers, MnO_x/SnO_2, with similar *N* and layer thickness as the first Mn/SnO_2 series (see Table II). These multilayers present much sharper interfaces (Fig. 10) since the oscillations due to the bilayer remain visible for the sample with $N=75$ and manganese oxide layer thickness of 0.4 nm while in Mn/SnO_2 multilayers, the bilayer structure is detected only for Mn layers down to 1.2 nm. Moreover, interdiffusion thicknesses (estimated from SUPREX fits, Tables I and II) have quite lower values than in Mn/SnO_2 samples. The starting manganese oxide of the target was MnO but after sintering at 1200 °C in air the diffraction pattern corresponds to Mn_3O_4. Nevertheless, dif-

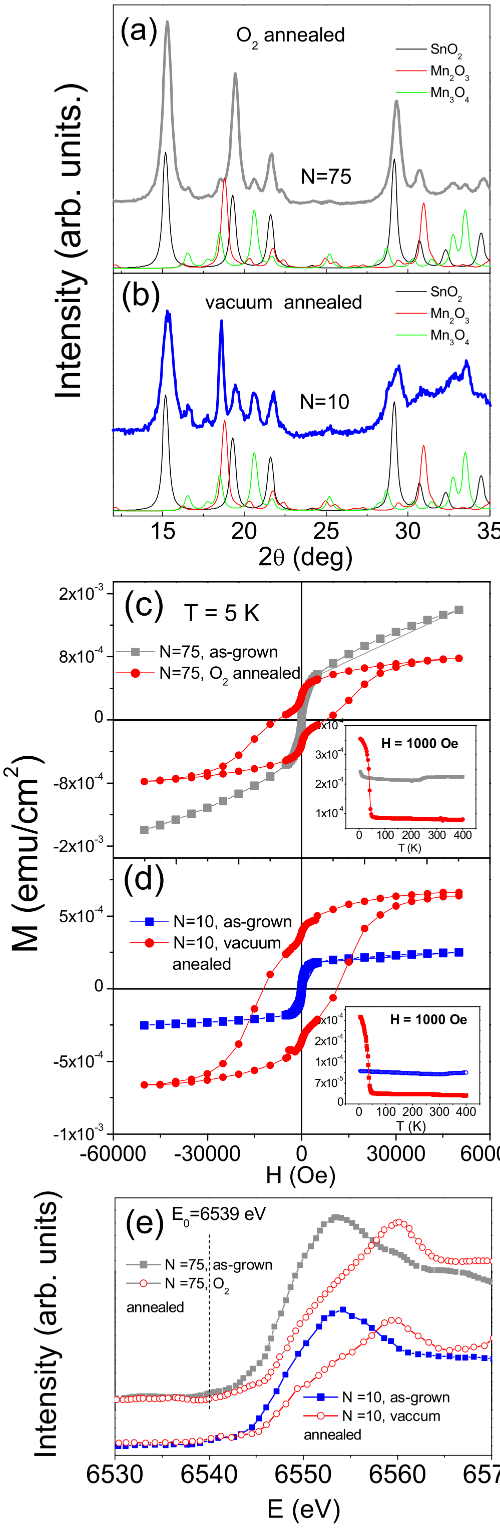

FIG. 8. (Color online) XRD patterns ($l=0.885$ Å) at low incidence of Mn/SnO_2 multilayers (a) annealed with O_2 ($N=75$) and (b) annealed in vacuum ($N=10$). References of SnO_2, Mn_2O_3, and Mn_3O_4 oxides are included. Magnetization (emu/cm^2) vs magnetic field (*H*) at 5 K of the above annealed Mn/SnO_2 multilayers, with O_2 (c) and in vacuum (d), compared with its respective as grown. (e) Mn *K*-edge XANES spectra for Mn/SnO_2 multilayer with $N=75$, as grown and O_2 annealed and $N=10$, as grown and vacuum annealed.

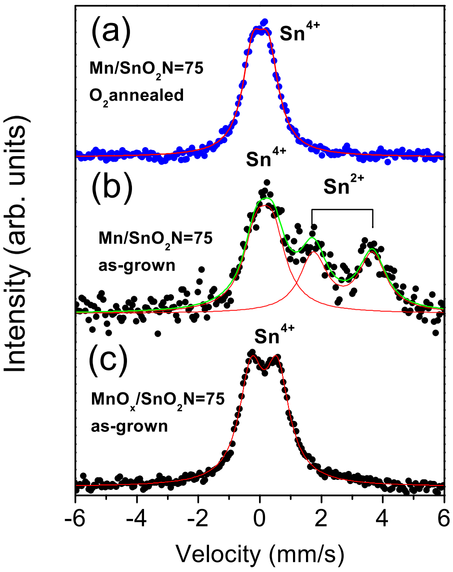

FIG. 9. (Color online) Mössbauer spectra for the Mn/SnO_2 multilayer with N=75 bilayers, O_2 annealed (a), as grown (b) and for the MnO_x/SnO_2 multilayer with N=75, as grown (c).

fraction data of the multilayers do not show the presence of Mn_3O_4 and magnetization data neither confirms the presence of this oxide, as it occurs in annealed Mn/SnO_2 multilayers. The Mn K edge [Fig. 10(a)] coincides with Mn^{3+}, therefore we have to infer that the multilayer is formed by Mn_2O_3 and SnO_2 [Mössbauer shows only Sn^{4+}, Fig. 9(c)] well defined not interdiffused layers.

The facility of Mn to bond oxygen, even in the almost O_2-free atmosphere of the sputtering chamber, explains the transformation from Mn_3O_4 of the sputtering target to Mn_2O_3 layers in these multilayers (this transformation requires one extra oxygen for six Mn). Therefore, the presence of Mn^{3+} does not guarantee the ferromagnetic interactions. The sharpness of the Mn_2O_3/SnO_2 interfaces as well as the valence state of Sn obtained by Mössbauer (only 4+) indicates that all Mn is forming the nonferromagnetic Mn_2O_3 oxide and in fact, the samples with N=5, 20, and 40 bilayers are mainly antiferromagnetic: the fits of the magnetization data to Brillouin functions give meaningless values of J_{PM}, between 0.1 and 1 depending on N, which can only be explained by the combination of an AF phase with a small paramagnetic fraction with $J_{PM}=2$ corresponding to Mn^{3+} ions. Only N=75 sample presents a different Mn valence (between 2+ and 3+) and paramagnetism related to diluted Mn [Fig. 11(b)]. It seems probable that the fraction of diluted Mn in SnO_2 is not enough to provide high-concentration regions of defects to order magnetically.

TABLE II. Parameters of MnO_x/SnO_2: number of bilayers (N), MnO_x layer thickness (d_{MnO_x}), SnO_2 layer thickness (d_{SnO_2}), bilayer thickness ($d_{bilayer}$), interdiffusion thickness ($\sigma_{A\text{-}B}$), and MnO_x content. Parameters fitted with SUPREX (thickness error ~5%).

N bilayers	d_{MnO_x} (nm)	d_{SnO_2} (nm)	$d_{bilayer}$ (nm)	d_{total} (nm)	$\sigma_{A\text{-}B}$ (nm)	% MnO_x content
5	11.0	3.2	14.5	75.7	0.2	64
20	2.5	3.2	5.7	117.2	0.2	42
40	1.2	3.0	4.2	171.0	0.4	26
75	0.4	3.0	3.4	258.0	0.5	11

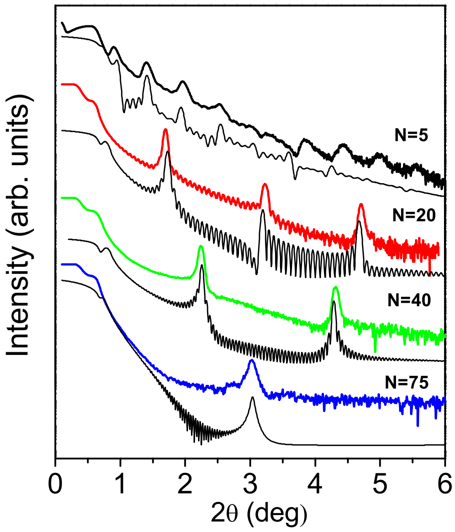

FIG. 10. (Color online) XRR measurements of MnO_x/SnO_2 multilayers with different number of bilayers N=5, 20, 40, and 75. SUPREX simulations of reflectivity are also displayed.

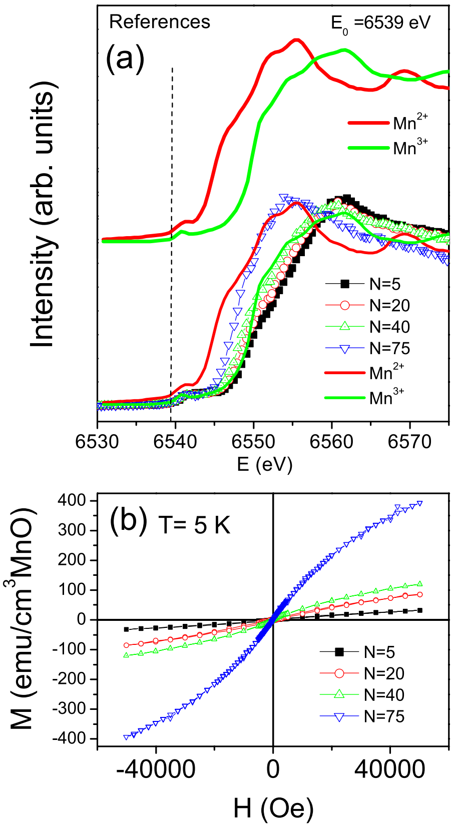

FIG. 11. (Color online) (a) Mn K-edge XANES spectra of reference MnO and Mn_2O_3 oxides (Mn^{2+}, Mn^{3+}) and of as-grown MnO_x/SnO_2 multilayers (N=5, 20, 40, and 75 bilayers). (b) Magnetization (M) vs magnetic field (H) at 5 K.

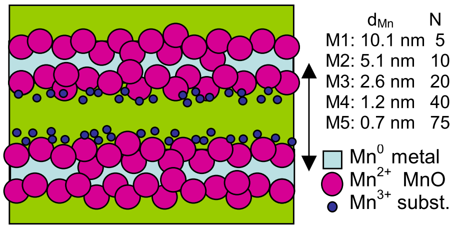

FIG. 12. (Color online) Schematic representation of Mn/SnO_2 multilayers with the different species of Mn deduced from the analysis of the experimental data.

In summary, the undoped SnO_2 films contain Sn exclusively in the 4+ valence state in any of the obtained phases (amorphous or polycrystalline) and a weak paramagnetic signal with an estimation of magnetic centers concentration of 10^{-3} centres/SnO_2 unit cell. Introducing metallic Mn layers produces Mn in different valence states (Fig. 12). One corresponds to Mn^{2+} (shown by XAS) which forms MnO nanocrystals (XRD) and produces an oxygen deficiency in SnO_2 layers which is mostly compensated by the formation of Sn^{2+} with the short-range order of SnO stable oxide. Interfaces with important interdiffusion, where Mn migrates into the Sn-O lattice, and exhibiting high Mn density regions are necessary for a ferromagnetic order which is based on short-range magnetic interactions mediated by the tin oxide lattice. Mn tends to form stable Mn oxides and no mixed Sn-Mn-O oxides are detected in any situation. Its combination with materials other than SnO_2 does not form ferromagnetic phases. Our explanation for all the previously described characteristics and behavior of the ferromagnetic signals is therefore related to the combination of Mn ions inside the tin oxide lattice in a metastable situation that is removed with a 10 min annealing but which is stable at room temperatures for months (at least). Mn^{3+} (an probably also 2+) located at Sn^{4+} sites may promote one (two) holes in the surrounding oxygen ions and a lattice relaxation that may favor ferromagnetic Mn-O-Sn-O-Mn coupling against the usual antiferromagnetic Mn-O-Mn superexchange in Mn oxides. This situation is similar to the deduced from the calculations of Ref. 33 and 45 where Sn vacancies[33] as well as Fe ions inside SnO_2 (Ref. 45) couple ferromagnetically. Both calculations obtain ferromagnetic coupling between defects (Sn vacancies or TM) for distances around 5 Å. Extrapolated to the present case, the observation of a cooperative ferromagnetic signal would require short Mn-Mn distances and a high number of such close Mn ions. Therefore in our samples is seems that the inhomogeneous Mn distribution inside tin oxide at the multilayer interfaces are able to produce regions of sufficient concentration and size to form long-range ferromagnetic order.

IV. CONCLUSIONS

The present study on SnO_2 films and multilayers combined with different compounds show that: (1) SnO_2 films show weak paramagnetic signal in their as-grown state. (2) When heavily doping with Mn, an important fraction of Sn^{2+} is detected. (3) The oxygen non stoichiometry is mainly compensated by the formation of tin mono-oxide (SnO). (4) Ferromagnetic phases require amorphous as-grown samples with high concentration of doping Mn cations. We conclude that intrinsic SnO_2 vacancies or interstitials are not enough to produce ferromagnetism due to the short-range mechanism which therefore requires high magnetic centers concentration regions. In SnO_2, the oxygen vacancies are at least partially compensated by the formation of SnO phase and therefore these are not expected to be relevant in this magnetism, nevertheless we cannot rule out completely the role of oxygen vacancies in ferromagnetism. The presence of Mn^{3+} (revealed by XAS) located at Sn^{4+} sites most probably produces a hole in the surrounding oxygen ions. These defects play the role of a Sn^{4+} vacancy in the previously mentioned calculations[33] giving rise to unpaired electrons at oxygen sites which mediate the ferromagnetic coupling between substitutional Mn. For particular conditions, the density of defects may be locally high enough to produce clusters of defects with superparamagnetic or ferromagnetic observable order. This ferromagnetic state seems to be unstable since annealing at 750 °C, either in reducing or oxidizing atmosphere, produce a clear decrease in the ferromagnetic signal and the formation of stable Mn oxides. Nevertheless the samples stored at room temperature for months do not show any evolution.

ACKNOWLEDGMENTS

This work has been supported by CSIC and by the Spanish “Ministerio de Educación y Ciencia” under the Contract No. MAT2009-08786. We thank ESRF for beamtime and BM25 personnel for technical support. The authors are also grateful to Ángel Muñoz, for his assistance in carrying out the RBS measurements.

---

[1] S. A. Chambers and S. Thevuthasan, Appl. Phys. Lett. **79**, 3467 (2001).

[2] S. R. Shinde, S. B. Ogale, S. Das Sarma, J. R. Simpson, H. D. Drew, S. E. Lofland, C. Lanci, J. P. Buban, N. D. Browning, V. N. Kulkarni, J. Higgins, R. P. Sharma, R. L. Greene, and T. Venkatesan, Phys. Rev. B **67**, 115211 (2003).

[3] K. Ueda, H. Tabata, and T. Kawai, Appl. Phys. Lett. **79**, 988 (2001).

[4] P. Sharma, A. Gupta, K. V. Rao, F. J. Owens, R. Sharma, R. Ahuja, J. M. O. Guillen, B. Johansson, and G. A. Guerin, Nature Mater. **2**, 673 (2003).

[5] S. B. Ogale, R. J. Choudhary, J. P. Buban, S. E. Lofland, S. R. Shinde, S. N. Kale, V. N. Kulkarni, J. Higgins, C. Lanci, J. R. Simpson, N. D. Browning, S. Das Sarma, H. D. Drew, R. L. Greene, and T. Venkatesan, Phys. Rev. Lett. **91**, 077205 (2003).

[6] J. M. D. Coey, A. P. Douvalis, C. B. Fitzgerald, and M. Venkate-

san, Appl. Phys. Lett. **84**, 1332 (2004).

[7] A. Punnoose, J. Hays, V. Gopal, and V. Shutthanandan, Appl. Phys. Lett. **85**, 1559 (2004).

[8] C. B. Fitzgerald, M. Venkatesan, L. S. Dorneles, R. Gunning, P. Stamenov, J. M. D. Coey, P. A. Stampe, R. J. Kennedy, E. C. Moreira, and U. S. Sias, Phys. Rev. B **74**, 115307 (2006).

[9] Y. Xiao, S. Ge, L. Xi, Y. Zuo, X. Zhou, B. Zhang, L. Zhang, C. Li, X. Han, and Z. Wen, Appl. Surf. Sci. **254**, 7459 (2008).

[10] K. Gopinadhan, S. C. Kashyap, D. K. Pandya, and S. Chaudharya, J. Appl. Phys. **102**, 113513 (2007).

[11] J. H. Park, M. G. Kim, H. M. Jang, S. Ryu, and Y. M. Kim, Appl. Phys. Lett. **84**, 1338 (2004).

[12] P. Sati, C. Deparis, C. Morhain, S. Schafer, and A. Stepanov, Phys. Rev. Lett. **98**, 137204 (2007).

[13] T. C. Kaspar, T. Droubay, S. M. Heald, M. H. Engelhard, P. Nachimuthu, and S. A. Chambers, Phys. Rev. B **77**, 201303(R) (2008).

[14] A. Espinosa, C. Prieto, M. García-Hernández, and A. de Andrés, J. Magn. Magn. Mater. **316**, e207 (2007).

[15] E. Céspedes, J. Garcia-Lopez, M. García-Hernández, A. de Andrés, and C. Prieto, J. Appl. Phys. **102**, 033907 (2007).

[16] T. C. Kaspar, S. M. Heald, C. M. Wang, J. D. Bryan, T. Droubay, V. Shutthanandan, S. Thevuthasan, D. E. McCready, A. J. Kellock, D. R. Gamelin, and S. A. Chambers, Phys. Rev. Lett. **95**, 217203 (2005).

[17] D. A. Schwartz and G. R. Gamelin, Adv. Mater. (Weinheim, Ger.) **16**, 2115 (2004).

[18] M. Gacic, G. Jakob, C. Herbort, H. Adrian, T. Tietze, S. Brück, and E. Goering, Phys. Rev. B **75**, 205206 (2007).

[19] N. Hoa Hong, N. Poirot, and J. Sakai, Phys. Rev. B **77**, 033205 (2008).

[20] J. M. D. Coey, M. Venkatesan, P. Stamenov, C. B. Fitzgerald, and L. S. Dorneles, Phys. Rev. B **72**, 024450 (2005).

[21] N. Hoa Hong, J. Sakai, and V. Brizé, J. Phys.: Condens. Matter **19**, 036219 (2007).

[22] T. Dietl, H. Ohno, F. Matsukura, J. Cibert, and D. Ferrand, Science **287**, 1019 (2000).

[23] A. Kaminski and S. Das Sarma, Phys. Rev. Lett. **88**, 247202 (2002).

[24] J. M. D. Coey, M. Venkatesan, and C. B. Fitzgerald, Nature Mater. **4**, 173 (2005).

[25] H. Iida, N. Shiba, T. Mishuku, A. Ito, H. Karasawa, M. Yamanaka, and Y. Hayashi, IEEE Electron Device Lett. **3**, 114 (1982).

[26] S. Semancik and R. E. Cavicchi, Thin Solid Films **206**, 81 (1991).

[27] H. Kimura, T. Fukumura, M. Kawasaki, K. Inaba, T. Hasegawa, and H. Koinuma, Appl. Phys. Lett. **80**, 94 (2002).

[28] A. Sundaresan, R. Bhargavi, N. Rangarajan, U. Siddesh, and C. N. R. Rao, Phys. Rev. B **74**, 161306(R) (2006).

[29] Ç. Kiliç and A. Zunger, Phys. Rev. Lett. **88**, 095501 (2002).

[30] A. Togo, F. Oba, I. Tanaka, and K. Tatsumi, Phys. Rev. B **74**, 195128 (2006).

[31] A. K. Singh, A. Janotti, M. Scheffler, and C. G. Van de Walle, Phys. Rev. Lett. **101**, 055502 (2008).

[32] Q. Wang, Q. Sun, G. Chen, Y. Kawazoe, and P. Jena, Phys. Rev. B **77**, 205411 (2008).

[33] G. Rahman, V. M. García-Suárez, and S. C. Hong, Phys. Rev. B **78**, 184404 (2008).

[34] X. F. Liu, Y. Sun, and R. H. Yu, J. Appl. Phys. **101**, 123907 (2007).

[35] L. A. Errico, M. Rentaría, and M. Weissmann, Phys. Rev. B **72**, 184425 (2005).

[36] C. E. Rodríguez Torres, L. Errico, F. Golmar, A. M. Mudarra Navarro, A. F. Cabrera, S. Duhalde, F. H. Sánchez, and M. Weissmann, J. Magn. Magn. Mater. **316**, e219 (2007).

[37] A. Espinosa, E. Céspedes, C. Prieto, M. García-Hernández, J. Rubio-Zuazo, and A. de Andrés, J. Appl. Phys. **103**, 07D129 (2008).

[38] A. Espinosa, N. Menendez, C. Prieto, and A. de Andrés, J. Non-Cryst. Solids **354**, 5269 (2008).

[39] E. E. Fullerton, I. K. Schuller, H. Vanderstraeten, and Y. Bruynseraede, Phys. Rev. B **45**, 9292 (1992).

[40] R. A. Brand, Nucl. Instrum. Methods Phys. Res. B **28**, 398 (1987).

[41] G. S. Collins, T. Kachnowski, N. Benczer-Koller, and M. Pasternak, Phys. Rev. B **19**, 1369 (1979).

[42] B. Stjerna, C. G. Grandvist, A. Seidel, and L. Häggström, J. Appl. Phys. **68**, 6241 (1990).

[43] We have used the following expression for the diffracted intensity from amorphous materials: $I \propto \Sigma_m \Sigma_n F_m(k) F_n(k) \frac{\sin(k \cdot r_{m-n})}{(k \cdot r_{m-n})}$, where $F_n(k)$ are the atomic factors and r_{m-n} the interatomic distances of the considered cluster.

[44] A Brillouin function with $J=100$ would correspond to superparamagnetic clusters but here we use it as a function that fits well the magnetization cycles of the long-range FM phase (except that it cannot account for the observed hysteresis) and allows to obtain the FM weight.

[45] S. Hu, S. Yan, X. Yao, Y. Chen, G. Liu, and L. Mei, Phys. Rev. B **75**, 094412 (2007).